

# Reconstructing Sunyaev–Zel’dovich clusters in future cosmic microwave background experiments

Elena Pierpaoli,<sup>1</sup>★ S. Anthoine,<sup>2</sup> K. Huffenberger<sup>3</sup> and I. Daubechies<sup>2</sup>

<sup>1</sup>California Institute of Technology, Mail Code 130–33, Pasadena, CA 91125, USA

<sup>2</sup>Department of Applied Mathematics, Princeton University, Princeton, NJ 08544, USA

<sup>3</sup>Physics Department, Princeton University, Princeton, NJ 08544, USA

Accepted 2005 January 28. Received 2004 November 24

## ABSTRACT

We present a new method for component separation aimed at extracting Sunyaev–Zel’dovich (SZ) galaxy clusters from multifrequency maps of cosmic microwave background (CMB) experiments. This method is designed to recover non-Gaussian, spatially localized and sparse signals. We first characterize the cluster non-Gaussianity by studying it on simulated SZ maps. We then apply our estimator on simulated observations of the *Planck* and Atacama Cosmology Telescope (ACT) experiments. The method presented here outperforms multifrequency Wiener filtering, both in the reconstructed average intensity for given input and in the associated error. In the absence of point source contamination, this technique reconstructs the ACT (*Planck*) bright (big) cluster central  $y$  parameter with an intensity that is about 84 (43) per cent of the original input value. The associated error in the reconstruction is about 12 and 27 per cent for the 50 (12) ACT (*Planck*) clusters considered. For ACT, the error is dominated by beam smearing. In the *Planck* case, the error in the reconstruction is largely determined by the noise level: a noise reduction by a factor of 7 would imply almost perfect reconstruction and 10 per cent error for a large sample of clusters. We conclude that the selection function of *Planck* clusters will strongly depend on the noise properties in different sky regions, as well as the specific cluster extraction method assumed.

**Key words:** galaxies: clusters: general – cosmic microwave background – large-scale structure of Universe.

## 1 INTRODUCTION

The study of the cosmic microwave background (CMB) has greatly improved our understanding of the Universe in the last decade. The measurement and interpretation of the CMB power spectrum has determined the most important cosmological parameters with very high accuracy (Spergel et al. 2003). More experiments, now planned or underway, will produce higher-resolution multifrequency maps of the sky in the 100–400 GHz frequency range. One of the most important new scientific goals of these experiments is the detection of clusters through their characteristic Sunyaev–Zel’dovich (SZ) signature (Sunyaev & Zel’dovich 1980). Because the SZ signal is substantially independent of redshift, SZ clusters above a mass threshold will be observed at very high distances. Such clusters may be used to infer cosmological information via number counts and power spectrum analysis of SZ maps (Levine, Schulz & White 2002; Battye & Weller 2003; Hu 2003; Majumdar & Mohr 2003; Weller & Battye 2003). These estimates, however, typically assume that all clusters above a given flux are perfectly reconstructed and detected

in the CMB maps. In practice, this may not be the case. SZ clusters have radio intensities comparable to other intervening cosmological signals such as the CMB and point sources, so disentangling them is difficult. Moreover, beam smearing and instrumental noise play a role in our ability to adequately reconstruct the observed cluster. For a given central Comptonization parameter  $y$  (see below for definition), the reconstructed value may also depend on the cluster location and shape. Given experimental specifications and a reconstruction technique, the associated reconstruction error needs to be assessed and accounted for when relating cluster observables to cosmological models. This error is in addition to that usually associated with cluster scaling relations, which play a major role in the current determination of  $\sigma_8$  from galaxy clusters (Pierpaoli et al. 2003).

Given the observed maps at different frequencies, clusters can be detected with two quite different approaches, as follows.

(i) A formal component separation is applied to the map, and the cluster map is reconstructed along with the maps for all other processes. This approach was initially developed to reconstruct CMB maps. Most often, it has been applied in Fourier space, with and without assumptions on the Gaussianity of the signal (Tegmark & Efstathiou 1996; Stolyarov et al. 2002).

★E-mail: pierpa@caltech.edu

(ii) The maps at different frequencies are first combined in an optimal way in order to enhance the cluster signal and minimize the others. A spatial filter (typically circularly symmetric) is then applied to the final map (Diego et al. 2002; Herranz et al. 2002).

Maps of clusters of galaxies present very specific features, the following in particular. (i) Clusters are ‘rare’ objects in the map; they do not fill the majority of the space. (ii) The cluster signal is non-Gaussian on several scales (Zhang, Pen & Wang 2002; Diego, Hansen & Silk 2003), and we are most interested in the non-Gaussianity on the scale of the typical cluster core size. (iii) The signal on different scales is correlated. Keeping these characteristics in mind, in this paper we develop a method for formal component separation of different signals that is tailored to better reconstruct the SZ galaxy cluster signal from multifrequency maps. Our map reconstruction method is wavelet-based and it can take into account the specific non-Gaussianity expected for a given signal (SZ clusters in particular). It can be seen that the combination of these two features enables us to better reconstruct the intensity of the cluster centre, which is essential to reliably relate the SZ signal to theoretical quantities in order to derive cosmological parameters.

Wavelets have been applied to the analysis of multifrequency maps to characterize specific signals (Starck, Aghanim & Forni 2004) and extract point sources (Cayón et al. 2000; Vielva et al. 2001a), to recover the CMB sky with maximum entropy methods (Vielva et al. 2001b; Masinger, Hobson & Lasenby 2004) and to assess statistics of the CMB (Hobson, Jones & Lasenby 1999; Tenorio et al. 1999; Cayón et al. 2001; Aghanim et al. 2003). Here, we focus on galaxy clusters, adopt a suitable wavelet basis, and develop a new Bayesian estimator appropriate to the reconstruction of the non-Gaussian signal associated with cluster maps (see Melin, Bartlett J. G. & Delabrouille 2005 for a matched filter analysis).

Future SZ surveys may be very different in nature. Space-based *Planck* will cover the whole sky, seeing all the most massive clusters but with relatively low resolution. A number of ground-based experiments will cover a smaller area with higher resolution. Because the performance of the reconstruction method also depends on the experimental characteristics, we apply our method to two different SZ experiments: the *Planck* surveyor and the Atacama Cosmology Telescope (ACT). The main purpose of this paper is to introduce our new estimator, on which component separation is based, and to test it and compare it with standard techniques. After reconstructing the SZ maps, we assess which error is involved in the determination of SZ observables from the map. The analysis of simulated maps allows us to design observables suited to derive cosmological parameters for a given experiment. We also assess the impact of instrumental limitations in recovering the cluster maps. We then assess the level of completeness and purity of the surveys for different flux cuts. Throughout the paper we compare our method with the standard multifrequency Wiener filtering technique applied in the same wavelet space.

This paper is organized as follows. In Section 2 we describe the relevant signals at radio/infrared frequencies and the characteristics of the experiments that we are going to consider. We then describe our wavelet basis and reconstruction method in Section 3. Section 4 is dedicated to the results and Section 5 to the conclusions.

## 2 ASTROPHYSICAL SIGNALS AND INSTRUMENT CHARACTERISTICS

We consider experiments that provide a map of the sky in the frequency range 100–400 GHz. In this range we expect to observe

several galactic and extragalactic signals, such as the synchrotron and dust emission from the Galaxy, the CMB, radio and infrared point sources and SZ galaxy clusters. We are interested here in the reconstruction of the cluster signal. Because the galactic signal has a very different spatial structure from SZ clusters, we assume here that the Galaxy is not a fundamental limitation in reconstructing SZ cluster maps, which is likely true in substantial portions of the sky. Point sources, particularly dusting star-forming galaxies at high-redshift which shine brightly at submm frequency, may be a potential concern. The modelling of source number counts, frequency dependences and spatial correlations remain uncertain. We prefer to leave them out of the analysis at the present time, and to test our technique in absence of point sources. For *Planck*, this approach is justified by the presence of higher- and lower-frequency channels, which will hopefully allow modelling and subtraction of point sources before component separation. For ACT, which lacks these channels, this is probably a too optimistic assumption (Huffenberger & Seljak 2004; White & Majumdar 2004). However, we use it for simplicity in testing our new estimator, which in any case we find to be superior to Wiener filtering techniques used previously. We will assess in future work the contamination of such sources in the context of the technique presented here.

We simulate the CMB with Gaussian random fields using a power spectrum derived from the best-fitting *Wilkinson Microwave Anisotropy Probe* (WMAP) parameters (Bennett et al. 2003).

In the following we review the SZ cluster signal and describe the characteristics of the simulated maps and of the experiments we are discussing here.

### 2.1 Clusters of galaxies

CMB photons travelling from the last scattering surface to the Earth interact with the high-energy electrons in intervening massive galaxy clusters. As a consequence of this scattering, the CMB temperature and intensity is modified in the direction of a cluster. These are known as the thermal and kinetic SZ effects. The effect related to the electron’s thermal motion causes a change in the CMB intensity  $\delta I$  in the direction  $\hat{n}$  of the cluster

$$\delta I(\hat{n}) = -2y(\hat{n})I_0S_I[x(\nu)], \quad (1)$$

where

$$S_I = \frac{x^4 \exp(x)}{[\exp(x) - 1]^2} \left[ 2 - \frac{x \exp(x) + 1}{2 \exp(x) - 1} \right]. \quad (2)$$

Here,  $x \equiv h\nu/k_B T_{\text{CMB}} = \nu/57 \text{ GHz}$ ,  $I_0 \equiv 2(k_B T_{\text{CMB}})^3/(hc)^2$  and

$$y(\hat{n}) = \frac{\sigma_T}{m_e c^2} \int_0^L n_e(l\hat{n}) k_B T_e(l\hat{n}) dl = \frac{\sigma_T}{m_e c^2} \int_0^L P_e(l\hat{n}) dl \quad (3)$$

is the Comptonization  $y$  parameter, which depends on temperature ( $T_e$ ) and number density ( $n_e$ ) through the pressure ( $P_e$ ) of free electrons. The integral is over the proper distance  $l$ . The corresponding temperature change is

$$\frac{\delta T_{\text{CMB}}}{T_{\text{CMB}}} = -2y(\hat{n}) \left[ 2 - \frac{x \exp(x) + 1}{2 \exp(x) - 1} \right]. \quad (4)$$

Note that in the Rayleigh–Jeans limit ( $x \ll 1$ ) we have  $\delta T_{\text{CMB}}/T_{\text{CMB}} = \delta I_\nu/I_\nu = -2y(\hat{n})$ . The thermal SZ signal causes a decrement (increment) of the intensity below (above) the characteristic frequency of 217 GHz. The thermal SZ is observable between 10 and 800 GHz, with a minimum (maximum) around 145 (350) GHz. Because of this peculiar frequency dependence, multifrequency observations are crucial in recovering the cluster SZ

**Table 1.** The characteristics of the *Planck* and ACT experiments at the frequencies used in this work. The rms detector noise per FWHM pixel, labelled  $\sigma$ , is given in thermodynamic temperature units.

Experiment	$\nu$ (GHz)	FWHM (arcmin)	$\sigma$ ( $\mu$ K)
<i>Planck</i>	143	7.1	6
	217	5.0	13
	353	5.0	40
ACT	145	1.7	2
	217	1.1	3.3
	265	0.93	4.7

signal. Massive clusters have typical  $y$  parameters of the order of  $10^{-4}$ , creating an SZ signal of the same order of magnitude as that of the CMB fluctuations.

The interaction of free electrons in galaxy clusters with the CMB photons is also responsible for the kinetic SZ. Clusters of galaxies have a peculiar motion with respect to the Hubble flow. As a consequence, the scattered CMB photons are subject to a Doppler effect due to the bulk cluster motion. The kinetic SZ is weaker than the thermal SZ and it has a similar frequency dependence to the CMB; therefore, it is harder to detect and separate from the CMB. Very likely, the kinetic SZ will be measured after cluster positions have been determined. We therefore ignore it in the component separation technique developed in the following sections.

## 2.2 Characteristics of future cosmic microwave background experiments

The performance of any component separation technique also depends on the characteristics of the experiment in hand. Future SZ surveys will have a broad spectrum of possible characteristics in terms of frequency coverage, sensitivity and resolution. For this reason, we specify here our analysis for two future CMB experiments that are very different in nature: *Planck*<sup>1</sup> and ACT.<sup>2</sup> The specifications for these experiments most relevant for SZ surveys are summarized in Table 1.

*Planck* is an all-sky experiment with a quite broad beam (5 arcmin) if compared to the typical cluster size (1–10 arcmin); therefore, we expect *Planck* to detect the most massive (or extended) clusters only. The large area covered, however, will allow us to detect a sizable number of them.

ACT is a higher-resolution, ground-based experiment where most massive clusters are larger than the beam. At this resolution, clusters appear aspherical (see Fig. 5, below, first panel) and the challenge here is also to be able to individually detect merging structures and resolve the outskirts of massive clusters. Moreover, we want to find the many small clusters which may be confused with noise (or other point sources).

In our simulations of both experiments, the detection of the cluster central emission is challenged by the following factors: (i) smearing by the instrumental beam; (ii) instrumental noise; (iii) confusion with the CMB anisotropy structure.

In the following we assess how precise the reconstruction is of the central emission in these experiments. In order to do so, we have constructed simulated maps of the sky at different frequencies for

both experiments with CMB and SZ cluster maps. For *Planck*, the  $10 \times 10$  deg<sup>2</sup> SZ cluster maps were taken from White (2003).<sup>3</sup> For ACT, we use  $1.19 \times 1.19$  deg<sup>2</sup> maps obtained from hydrodynamical simulations by Zhang et al. (2002). For both experiments, the reconstruction was based on three frequency channels, which are specified in Table 1.

## 3 RECONSTRUCTION METHOD

In this section, we present the method used to reconstruct the different processes from the observed maps. Instead of the usual Fourier space decomposition of the signal, we adopt here a wavelet decomposition. We perform a Bayesian least-squares estimation of the different processes, modelling the statistics of wavelet coefficients of the signals by Gaussian scale mixtures. The estimation can be thought of as weighted local Wiener filters on neighbourhoods of wavelet coefficients, where the weight is determined by the specific non-Gaussianity under consideration. Below, we describe the details of the wavelet choice, and of the reconstruction method.

### 3.1 Wavelet decomposition used

Because we deal with sky maps, we are interested in two-dimensional wavelets. In the choice of the wavelet to use for our image processing, we have to balance the orthogonality of the wavelet (which is desirable in order to define well the statistics) with the compatibility of the wavelet with the image at hand. Orthogonal wavelet bases, such as the two-dimensional Daubechies wavelets, are typically heavily biased towards horizontal and vertical directions; moreover, they are usually not very well concentrated in frequency. To avoid this, we use an overcomplete wavelet representation inspired by the work of Portilla, Strela & Wainwright (2003), which is more adequate to the analysis of astrophysical images.

The wavelet decomposition of a signal  $s$  in our case is

$$s = \sum_{q \in Z^2} \langle s, \phi_q \rangle \phi_q + \sum_{j=0}^J \sum_{m=1}^M \sum_{q \in 2^{-j} Z^2} \langle s, \psi_{j,m,q} \rangle \psi_{j,m,q} \quad (5)$$

where  $\phi_q$  are the scaling functions,  $\psi_{j,m,q}$  are the wavelets and  $\langle \cdot \rangle$  are scalar products. The sum  $\sum_q \langle s, \phi_q \rangle \phi_q$  is the projection of  $s$  on the coarsest scale, i.e. a low-pass version of  $s$ . Each scaling coefficient  $\langle s, \phi_q \rangle$  contains information about the signal  $s$  at the coarsest scale and at a specific location in space  $q$ . For  $j$  fixed, the sum  $\sum_m \sum_q \langle s, \psi_{j,m,q} \rangle \psi_{j,m,q}$  is the projection of  $s$  on the scale  $j$ , i.e. a bandpass version of  $s$ . Each wavelet coefficient  $\langle s, \psi_{j,m,q} \rangle$  contains information about the signal  $s$  at the specific scale  $j$ , orientation  $m$  and location in space  $q$ .

As usual with wavelet transforms, changing scale is done by dilating, and changing location is done by translating the wavelet:

$$\psi_{j+1,m,q}(x) = 2\psi_{j,m,q}(2x), \quad \psi_{j,m,q}(x) = \psi_{j,m,0}(x - q). \quad (6)$$

Hence, scale  $j + 1$  corresponds to a spatial frequency band that is twice as wide, and for which the central frequency is twice as large, as that of scale  $j$ . On the other hand, in space, the wavelets at scale  $j + 1$  are better localized than at scale  $j$  because they are more narrowly concentrated around their centre  $q$  (see Fig. 1, columns 1 and 2).

Unlike the two-dimensional Daubechies wavelets, the wavelets (and scaling function) we use here are defined in the Fourier plane. This ensures that they are well concentrated in frequency. Moreover, it enables us to introduce orientation by rotating the Fourier

<sup>1</sup> See <http://planck.esa.int/>.

<sup>2</sup> See <http://www.hep.upenn.edu/act/index.html>.

<sup>3</sup> See <http://pac1.berkeley.edu/tSZ/PlanckSZ/>.



**Figure 1.** Top row: wavelets in space. Bottom row: wavelets in the Fourier plane. First column: wavelet at a fine scale  $j + 1$ , centred at location  $q_0$ , oriented along the first diagonal. Second column: wavelet at a coarser scale  $j$ , centred at location  $q_1$ , oriented along the first diagonal. Third column: wavelet at the same coarser scale  $j$ , centred at location  $q_2$ , oriented along the horizontal axis. Fourth column: scaling function, centred at location  $q_2$ .

transform of the wavelet (see Fig. 1, columns 2 and 3). If  $\tilde{f}$  is the Fourier transform of  $f$  and  $(r, \theta)$  are polar coordinates, then

$$\widetilde{\psi_{j,m,q}}(r, \theta) = \widetilde{\psi_{j,0,q}}\left(r, \theta - \frac{m\pi}{M}\right). \quad (7)$$

The transform is therefore close to rotation invariant and computation is fast via fast Fourier transform (FFT).

The Fourier transform of the wavelets and scaling functions are

$$\begin{aligned} \widetilde{\phi}_0(r, \theta) &= L(2r, \theta) \\ \widetilde{\psi_{j,m,0}}(r, \theta) &= L\left(\frac{r}{2^j}\right) H\left(\frac{2r}{2^j}\right) G_M\left(\theta - \frac{m\pi}{M}\right) \end{aligned} \quad (8)$$

for  $j \geq 0$ , and  $0 \leq m < M$ , where the low-pass filter  $L(r)$ , the high-pass filter  $H(r)$  and the oriented filters  $G_M(\theta)$  are

$$\begin{aligned} L(r) &= \cos\left[\frac{\pi}{2} \log_2(r)\right] \delta_{1 < r < 2} + \delta_{r < 1} \\ H(r) &= \sin\left[\frac{\pi}{2} \log_2(r)\right] \delta_{1 < r < 2} + \delta_{r > 2} \\ G_M(\theta) &= \frac{(M-1)!}{\sqrt{M} [2(M-1)]!} |2 \cos \theta|^{M-1}. \end{aligned} \quad (9)$$

The set of all wavelets and scaling functions determines a redundant system (they are linearly dependent). However, the Plancherel equation holds:

$$\|s\|_{L_2}^2 = \sum_{q \in \mathbb{Z}^2} |\langle s, \phi_q \rangle|^2 + \sum_{j=0}^J \sum_{m=1}^M \sum_{q \in 2^{-j} \mathbb{Z}^2} |\langle s, \psi_{j,m,q} \rangle|^2. \quad (10)$$

This ensures perfect reconstruction (equation 5).

Given an image  $s$ , it is possible to define a wavelet power spectrum  $P_w$ , which is related to the Fourier-based power spectrum  $P(k) = |\tilde{s}(k)|^2$ :

$$P_w(j) = \sum_{m,q} \frac{|\langle s, \psi_{j,m,q} \rangle|^2}{2^{2j}} = \sum_m \int P(k) \frac{|\widetilde{\psi_{j,m,0}}(k)|^2}{2^{2j}} dk. \quad (11)$$

The Fourier power spectra (in  $\mu\text{K}^2$ ) for the relevant signals (CMB, SZ clusters and noise) are displayed in Fig. 2 (left panel) together with the windows of wavelets at different scales. The right panel shows the corresponding wavelet spectra.

### 3.2 Estimator

Formally, our goal is to estimate several processes (CMB and SZ) from their contributions in observations at different frequencies. We

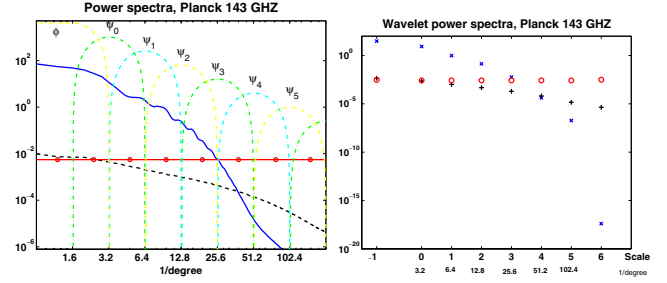


**Figure 2.** Left: power spectra in Fourier space of the wavelets at different scales (dash-dotted line) and signals : CMB (solid line), clusters (dashed line) and noise (solid line with circles) for *Planck* at 143 GHz. Note that here we only index the scale of the wavelet. Right: corresponding power spectra in wavelet space for the CMB (crosses), clusters (plus symbols) and noise (circles) for *Planck* at 143 GHz.

estimate the processes  $\{x(p, \nu_0)\}_p$  from the observations  $\{y(\nu)\}_\nu$  given that

$$y(\nu) = \sum_p f(p, \nu) x(p, \nu_0) * B(\nu) + N(\nu). \quad (12)$$

Here,  $x(p, \nu_0)$  is the template of the  $p$ th process at a given frequency  $\nu_0$ ,  $f(p, \nu)$  is the frequency dependence of the  $p$ th process,  $B(\nu)$  is the beam (assumed to be a Gaussian with given FWHM) and  $N(\nu)$  is the frequency-dependent white noise.

In wavelet space, these equations look similar: the observed wavelet coefficients  $\langle y(\nu), \psi_{j,m,q} \rangle = y_{j,m,q}(\nu)$  are linear combinations of the wavelet coefficients of the different processes  $x_{j',m',q'}(p, \nu_0)$ .

Our estimation method relies on two principles to discriminate the contributions from different processes. The first is that we know some statistical properties of the processes (e.g. the CMB and noise are Gaussian processes, while the clusters are not). The second is that some spatial properties of the processes can be captured by modelling the coherence of wavelet coefficients (Romberg et al. 2003). For example, clusters can be described as spatially localized structures with a high-intensity peak. Hence, if a cluster is centred at location  $q_0$ , one should see rather big wavelet coefficients around this location through different scales. If there is no cluster there, all these coefficients should be fairly small. This would not be the case for the noise. We aim to a local reconstruction, which can take advantage of these correlations. In order to estimate a particular wavelet coefficient  $x_{j,m,q}$ , we consider a neighbourhood of coefficients around it:

$$\mathbf{x} \equiv \mathbf{x}_{j,m,q} = (x_{j,m,q}, x_{j,m,q+1}, x_{j,m,q-1}, x_{j-1,m,q}). \quad (13)$$

Such a neighbourhood contains wavelet coefficients at the same scale with close location, and at a close scale with the same location.

Furthermore, we choose to statistically describe the signal as a Gaussian scale mixture (Portilla et al. 2003)

$$\mathbf{x} \equiv \sqrt{z} \mathbf{u} \quad (14)$$

where  $\mathbf{u}$  is a centred Gaussian vector of the same covariance as  $\mathbf{x}$  ( $\mathbf{C}_x = \mathbf{C}_u$ ), the multiplier  $z$  is a scalar random variable (whose distribution we prescribe later) and the equality holds in distribution. The variables  $\mathbf{u}$  and  $z$  are independent and  $E\{z\} = 1$ . The covariance of  $\mathbf{x}$  captures the spatial coherence of the process, while the (non-)Gaussianity of the signal is captured by the distribution of the multiplier  $z$ . We take the covariance  $\mathbf{C}_x$  to be a function of the scale  $j$  and orientation  $m$ . The convenience of this signal's description will be more clear in the next section.

### 3.2.1 Step one: denoising one observation of one process

To illustrate the idea for the reconstruction process, let us first consider the simple case where we observe one process polluted by noise:  $y(v_0) = x(v_0) + N(v_0)$ . The equations for each single wavelet coefficient and for the neighbourhood of wavelets coefficient are

$$y_{j,m,q} = x_{j,m,q} + N_{j,m,q} \quad (15)$$

$$\mathbf{y} = \mathbf{x} + \mathbf{N}$$

where  $N$  is Gaussian and  $\mathbf{x}$  is described with the Gaussian mixture in equation (14). The convenience of this representation is that for a fixed multiplier  $z = z_0$ , the Bayes least-squares estimate of  $\mathbf{x}$ , given the observed vector  $\mathbf{y}$  and  $z$ , would be a Wiener filter on the neighbourhood of wavelet coefficients:

$$E\{\mathbf{x}|\mathbf{y}, z = z_0\} = z_0 \mathbf{C}_x (z_0 \mathbf{C}_x + \mathbf{C}_N)^{-1} \mathbf{y}. \quad (16)$$

However, in our model  $z$  is not a constant, so  $E\{\mathbf{x}|\mathbf{y}\}$ , the Bayes least-squares estimate of  $\mathbf{x}$ , is a weighted average of the Wiener filters above:

$$E\{\mathbf{x}|\mathbf{y}\} = \int_0^\infty p(z = z_0|\mathbf{y}) E\{\mathbf{x}|\mathbf{y}, z = z_0\} dz_0. \quad (17)$$

The weights are determined by the probability of  $z$  given the observation  $\mathbf{y}$ , noted  $p(z = z_0|\mathbf{y})$ , which is computed via the Bayes rule

$$p(z = z_0|\mathbf{y}) = \frac{p(\mathbf{y}|z = z_0)p_z(z_0)}{\int p(\mathbf{y}|z = z')p_z(z') dz'}, \quad (18)$$

where  $p(\mathbf{y}|z = z')$  is a centred Gaussian vector of covariance  $z' \mathbf{C}_x + \mathbf{C}_N$ , and  $p_z$  is the probability distribution of  $z$ , which we describe in Section 3.3.

Following this procedure, we obtain an estimate  $E\{\mathbf{x}|\mathbf{y}\}$  for each neighbourhood of coefficients  $\mathbf{x}$ . From this estimated vector, we only keep the estimate of central coefficient  $x_{j,m,q}$ .

### 3.2.2 Step two: deblurring one observation of one process

Consider now the case where the observed signal is a blurred version of the original:  $y(v_0) = x(v_0) * B(v_0) + N(v_0)$ . The convolution with the beam correlates the signal spatially. As a result, a single observed wavelet coefficient is dependent on many wavelet coefficients in the signal. The equations no longer decouple:

$$y_{j,m,q} = \sum_{q'} B\left(\frac{q' - q}{2^j}\right) x_{j,m,q'} + N_{j,m,q}. \quad (19)$$

Because support of the beam is infinite, every wavelet coefficient  $x_{j,m,q'}$  contributes to  $y_{j,m,q}$ . However, the biggest contribution comes from the wavelet coefficients at a close location ( $|q - q'|$  small). Hence, if the size of the neighbourhood is big enough, we can make the following approximation

$$y_{j,m,q} = \mathbf{B}_j \mathbf{x}_{j,m,q} + N_{j,m,q}, \quad (20)$$

where  $\mathbf{B}_j$  is a matrix which depends on the beam  $B$  and the scale. Equations (17) and (18) hold with the modified Wiener filter

$$E\{\mathbf{x}|\mathbf{y}, z = z_0\} = z_0 \mathbf{C}_x \mathbf{B}_j^* (z_0 \mathbf{B}_j \mathbf{C}_x \mathbf{B}_j^* + \mathbf{C}_N)^{-1} \mathbf{y}, \quad (21)$$

and the covariance of  $p(\mathbf{y}|z = z')$  is now  $z' \mathbf{B}_j \mathbf{C}_x \mathbf{B}_j^* + \mathbf{C}_N$ .

The matrix  $\mathbf{B}_j$  is a truncated version of the matrix of convolution by the beam projected at scale  $j$ . For equation (20) to be a good approximation, we allow the size of the neighbourhood of wavelet coefficients to vary with the scale. Specifically, we extend the neighbourhood of equation (13) so that we capture 90 per cent

of the power of the beam at each scale. To do this, we simply include in  $\mathbf{x}_{j,m,q}$  the coefficients  $x_{j,m,q'}$ , with  $|q' - q| < k$ , choosing  $k$  so that  $\sum_{|q' - q| < k} |B(q'/2^j)|^2 > 0.9$ . Note that the coarser the scale, the smaller  $k$  is.

### 3.2.3 Step three: demixing several processes from several observations

We can extend this procedure to the case where several processes contribute to signals observed at different frequencies, as in equation (12).

For each process  $x(p, v_0)$ , each neighbourhood of wavelet coefficients is modelled as a Gaussian scale mixture

$$\mathbf{x}_{j,m,q}(p) \equiv \sqrt{z_{j,m,q}(p)} \mathbf{u}_{j,m,q}(p), \quad (22)$$

where  $z(p)$  are scalars of mean 1,  $\mathbf{u}(p)$  are Gaussian vectors, and all these random variables are independent. The approximation in equation (20) for a neighbourhood of wavelet coefficients is now

$$y_{j,m,q}(v) = \sum_p f(p, v) \mathbf{B}_j(v) \mathbf{x}_{j,m,q}(p) + N_{j,m,q}(v). \quad (23)$$

Assuming we have  $K$  observations and  $P$  processes, we note  $\mathbf{Y} = [y_{j,m,q}(v_1), \dots, y_{j,m,q}(v_K)]$  and  $\mathbf{Z} = [z(1), \dots, z(P)]$ . If  $\mathbf{Z}$  is fixed, we obtain a multicomponent Wiener filter on neighbourhood of wavelet coefficients

$$E\{\mathbf{x}(p)|\mathbf{Y}, \mathbf{Z}\} = z(p) \mathbf{C}_{x(p)} \sum_{k,k'=1}^K f(p, v_k) \mathbf{B}_j^*(v_k) \mathbf{G}_{k,k'}^{-1} \mathbf{y}'(v'_k) \quad (24)$$

where

$$\mathbf{G}_{k,k'} = \sum_{p=1}^P z(p) f(p, v_k) f(p, v_{k'}) \mathbf{B}_j(v_k) \mathbf{C}_{x(p)} \mathbf{B}_j^*(v_{k'}) + \delta_{k=k'} \mathbf{C}_{N(v_k)}. \quad (25)$$

The Bayes least-squares estimate of the full model is

$$E\{\mathbf{x}(p)|\mathbf{Y}\} = \int_{R_+^P} p(\mathbf{Z}|\mathbf{Y}) E\{\mathbf{x}(p)|\mathbf{Y}, \mathbf{Z}\} dz_1 dz_2 \dots dz_P \quad (26)$$

with the weights

$$p[\mathbf{Z} = (\alpha_i)_i | \mathbf{Y}] = \frac{p[\mathbf{Y}|\mathbf{Z} = (\alpha_1, \dots, \alpha_P)] \prod p_{z_i}(\alpha_i)}{\int p[\mathbf{Y}|\mathbf{Z} = (\beta_1, \dots, \beta_P)] \prod p_{z_i}(\beta_i) d\beta_i} \quad (27)$$

where  $p[\mathbf{Y} = \mathbf{y}(v_k)_k | \mathbf{Z} = (\alpha_i)_i]$  is a centred Gaussian with covariance matrix  $\mathbf{G}_{k,k'}$ .

In practice we compute the Bayes least-squares estimate for each wavelet neighbourhood  $\mathbf{x}$  and only keep the central coefficient  $x_{j,m,q}$  for each process. We then reconstruct the processes by inverting the wavelet transform.

In order to compute the estimate, we need the covariance matrices  $\mathbf{C}_{N(v)}$  and  $\mathbf{C}_{x(p)}$ . Note that these matrices depend on the scale and orientation. Because the level of noise is assumed to be known, the covariances  $\mathbf{C}_{N(v)}$  can be computed. The covariances for the different processes  $\mathbf{C}_{x(p)}$  are estimated from simulated input maps. We use the wavelet transform described in Section 3.1 with four orientations and five scales for the ACT experiment, and with four orientations and six scales for the *Planck* experiment. The size of the neighbourhoods is chosen adaptively at each scale so that the approximation in equation (23) is valid (as explained in Section 3.2.2). Finally, we choose the probability distributions  $p_{z_i}$  to capture the properties of the process  $x(i, v_0)$ , as noted in the next section.

### 3.3 Statistical properties of the signals

We now must decide which distribution  $p_z$  we intend to use for each signal. In the case where  $z \equiv 1$ , the Gaussian scale mixture described in equation (14) reduces to a Gaussian process. We are considering here that the CMB is Gaussian, and we consistently assume  $z \equiv 1$  at all scales for this signal.

The cluster signal however is typically non-Gaussian. In order to model such non-Gaussianity, we need a more elaborate distribution for  $z$ , which could in principle be chosen with or without any particular link to the true distribution. In the following we consider different cases for the cluster's  $z$  distribution (with and without a physical significance) and we compare the results.

In order to compute a physically based model for the cluster non-Gaussianity, we analysed the simulated SZ map. For the Gaussian scale mixture model of the signal, it is difficult to solve the closed-form equation for  $p_z$  (the probability of  $z$ ) given the probabilities of  $x$  and  $u$ . We instead study the probability of its logarithm,  $p_{\ln z}$ , and refer to it as the prior. Note that  $p_z$  can then be easily recovered:  $p_z(v) dv = p_{\ln z}(u) e^u du$  for  $u = \ln v$ . Taking the logarithm of equation (14), we obtain the following equation

$$p_{\ln|x|}(v) = \int_0^\infty 2p_{\ln z}(2y)p_{\ln|u|}(y-v) dy, \quad (28)$$

which we solve given that  $u$  is Gaussian and  $p_{\ln|x|}$  is estimated from the SZ input maps; details will be given in an upcoming paper (Anthoine, in preparation).

Together with the physical prior described above, we also consider two other non-physical priors: (i) the Gaussian prior, which corresponds to assuming  $z \equiv 1$ , or equivalently  $p_{\ln z}(v) = \delta_D(v-0)$ ; (ii) the non-informative prior, i.e. the uniform probability distribution on  $\ln z$ ,  $p_{\ln z}(v) = \text{constant}$ . The latter has been used for recovering non-Gaussian signals in digital image processing. We compare the performances of the non-informative and Gaussian priors to the one that we derived from the input maps.

We plot the distributions described above in Fig. 3 for the scale where the SZ signal is most pronounced. The behaviour of  $p_{\ln z}$  for small (large) values influences the probability of finding small (large) values of  $|x|$ . In our model,  $p_x$  describes the statistics of wavelet coefficients. Hence, the higher the probability  $p_x$  for small values of  $|x|$ , the sparser we expect the signal to be. The more pronounced the tails of  $p_x$  for large  $|x|$ , the more intense we expect the non-zero signal (i.e. the clusters) to be.

In Fig. 4, we plot the marginal distribution of the wavelet coefficients for SZ clusters as computed from the map, and we show how the different  $z$  priors in Fig. 3 would fit the actual distribution. The right panel shows that the tail of the cluster distribution is much broader than that of the Gaussian. As a consequence, the Gaussian prior tends to underestimate the amplitude of clusters. The left panel shows that the Gaussian prior underestimates the number of wavelet coefficients with small amplitude, while the non-informative prior and to some extent the profile prior overestimate them. This means that the sparsity of the cluster signal is not well described by these distributions. The Gaussian prior will tend to create more clusters than necessary while the non-informative prior or the profile will miss clusters.

We also discuss another case that is derived from the physical one: a truncated version of the  $p_{\ln z}$  estimated from the input maps (which we refer to as profile d). This version is a trade-off between the profile computed from the data and the Gaussian prior.

To summarize, in the rest of the paper we compare the results given by these four priors:

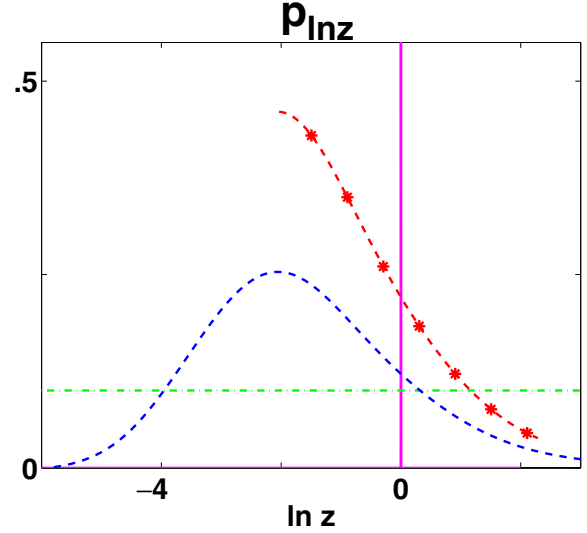


**Figure 3.** Examples of probability distribution for  $\ln z$  for a particular scale of the wavelet decomposition. Here  $z$  is the multiplier in the Gaussian scale mixture model. Solid line: Gaussian prior,  $p_{\ln z}(v) = \delta_D(v-0)$ ,  $z \equiv 1$ . Dash-dotted line: non-informative prior,  $p_{\ln z} \equiv \text{constant}$ . Dashed line: profile computed from the data. Dashed line with stars: profile computed from the data truncated (profile d).

- (i) Gaussian prior,  $p_{\ln z}(v) = \delta_D(v-0)$ , referred to as Gaussian;
- (ii) non-informative prior,  $p_{\ln z}(v) = \text{constant}$ , referred to as uniform;
- (iii) profile computed from the data, referred to as profile;
- (iv) truncated profile computed from the data, referred to as profile d.

## 4 RESULTS

### 4.1 Reconstructed maps

We applied the method described above to the ACT and *Planck* simulated maps with realistic beam and noise properties (see Table 1), with different assumptions on the prior  $p_{\ln z}$ . In Figs 5 and 6 we show the input and reconstructed  $y$  maps for ACT and *Planck*, respectively.

In these figures we notice that, even using a wavelet basis which allows for a local reconstruction, the Gaussian prior for  $p_{\ln z}$  (which causes the estimator to reduce to Wiener filtering on the neighbourhood of wavelet coefficients) underestimates the high-intensity peaks. In contrast, the profile and uniform prior perform (equally) better, reconstructing the central intensity of the bright clusters, indicating that the specific shape of the tail of the prior distribution of multipliers for high  $z$  is not particularly relevant, as long as it provides enough power at sufficiently high  $z$  values.

As for the low-intensity clusters, they seem better reconstructed in the Wiener filtered maps than by using the real profile (or uniform) prior for  $p_{\ln z}$ . This indicates that our estimate of the true  $p_{\ln z}$ , the profile, may be weighing too heavily low-intensity points. This effect could be caused by the procedure we adopt in computing  $p_{\ln z}$  from the input maps. Because of our deconvolution technique (see Section 3.3, equation 28), it may well be that if the true  $p_{\ln z}$  had a very sharp drop at some low  $z$  value, we would not be able to model it accurately. For this reason, we also tried a profile that

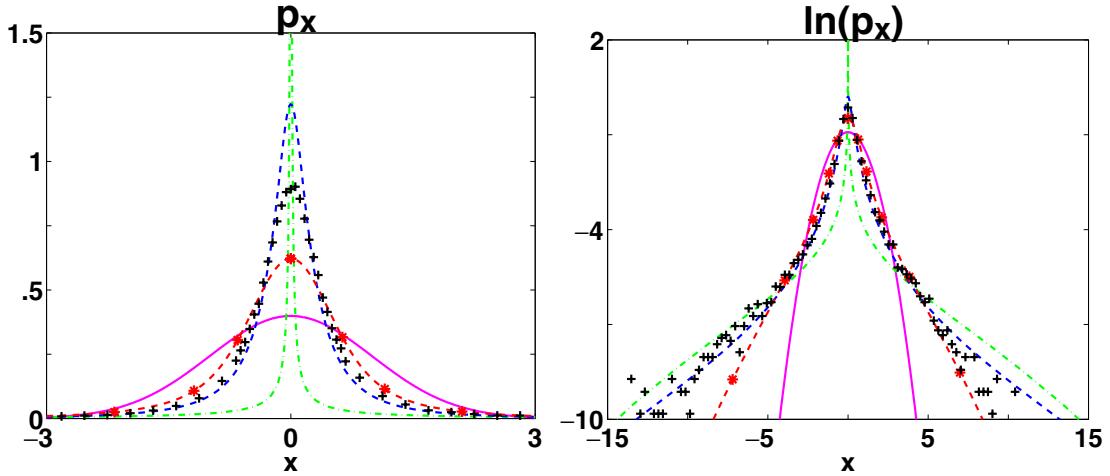


**Figure 4.** Top panel:  $p_x$ , the distribution of  $x \equiv \sqrt{z}u$ . Bottom panel: the logarithm of this distribution,  $\ln(p_x)$ . In order of increasing value of  $p_x$  at  $x = 0$  (left) and increasing value of  $|x|$  for  $\ln(p_x) = -10$  (right). Solid line: Gaussian prior,  $x$  is Gaussian. Dashed line with stars:  $p_x$  corresponding to the profile computed from the data truncated (profile d). Plus symbols: distribution  $p_x$  as numerically computed from the input maps. Dashed line:  $p_x$  corresponding to the profile computed from the data. Dash-dotted line:  $p_x$  corresponding to the non-informative prior.

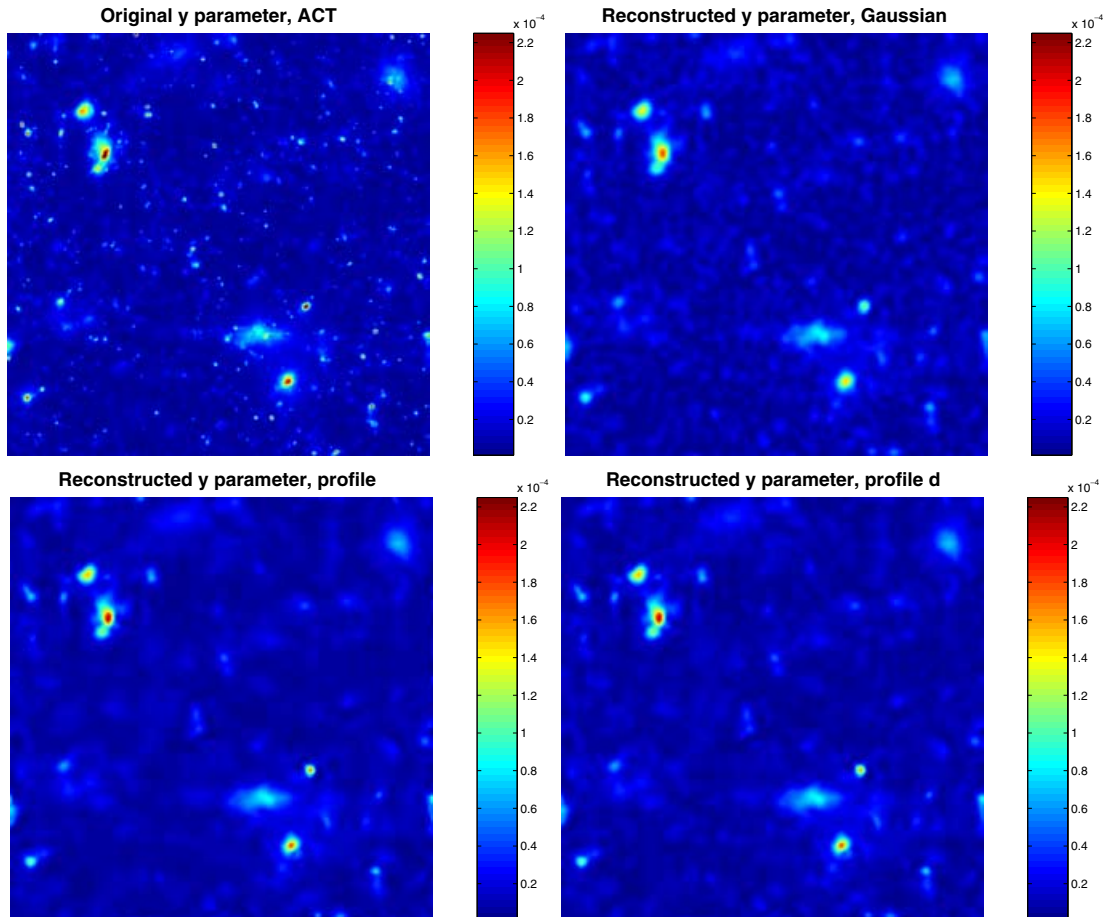


**Figure 5.** The simulated panel (top left) and reconstructed ACT cluster maps. The second panel (top right) corresponds to the Gaussian prior, the third (bottom left) to the actual cluster prior ‘profile’, and the fourth (bottom right) to the truncated cluster prior ‘profile d’. The maps is 1.2 deg on a side.

corresponds to the true one truncated at  $z$  lower than the peak point (see Fig. 3, profile d case). The truncated profile performs as well as Wiener filtering in recovering low-intensity clusters, still improving the results on high-intensity clusters.

#### 4.2 Central $y$ parameter

When it comes to inferring cosmological parameters from number counts in other wavebands (e.g. X-ray and optical) the common

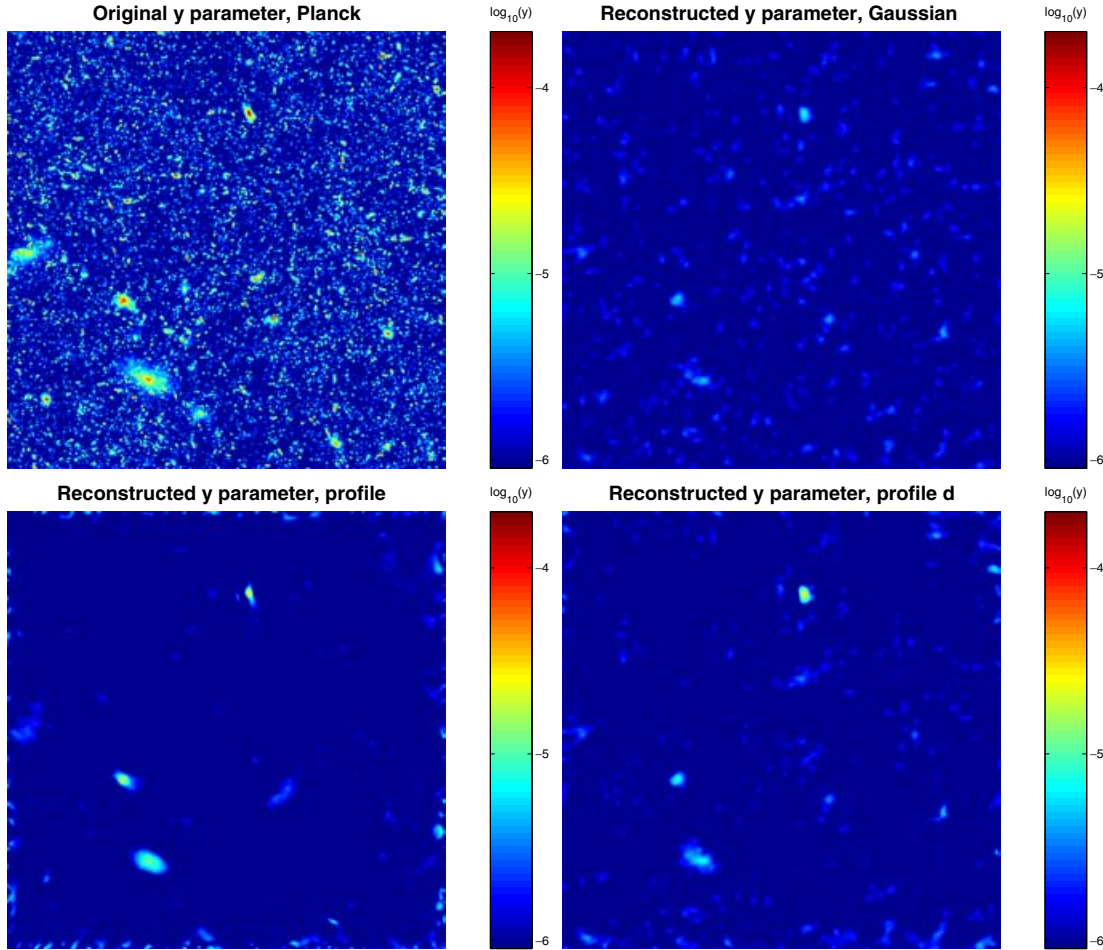


**Figure 6.** The original and reconstructed *Planck* cluster maps. The distributions are the same as the corresponding ACT panels. Note that the colour scale here is in the logarithm of the luminosity. Border effects are visible: the areas at the edges are disregarded in the analysis. The map is 10 deg on a side.

practice is to retain only the brightest clusters, which are less affected by selection effects and have a better characterized scaling function. We adopt the same strategy with SZ clusters, also motivated by the fact that they are less affected by reconstruction errors. For these clusters it is appropriate to assess how the input  $y$  parameter relates to the reconstructed  $y$  parameter. Figs 7 and 8 show the reconstructed versus input  $y$  parameter for ACT and *Planck*, respectively, smoothed over a scale which is roughly the smallest beam size in each experiment. In Table 2, we quote the slope of the fitting line for the different distributions considered, together with the average percentage departure from it, or spread, computed as the mean of the ratio:  $|(\text{input} - \text{predicted})/\text{input}|$  with  $\text{predicted} = \text{output} / \text{slope}$ . In general, using either the uniform or the profile prior for  $p_{\text{in},z}$  improves both the average reconstruction (the slope of the curve) and the associated error. The actual performance depends on the intensity cut applied; here, we plot the 50 brightest ACT clusters and the 12 *Planck* most extended clusters in the reconstructed maps (see Section 4.4 for a discussion on selection effects). In the case of ACT, the average reconstruction improves by about 20 per cent on the Gaussian prior case when our approach is applied using any of the three other distributions. The scatter is also reduced by a factor of 2. In the case of *Planck*, the improvement in the average reconstruction is roughly a factor of 5, and the error is also reduced.

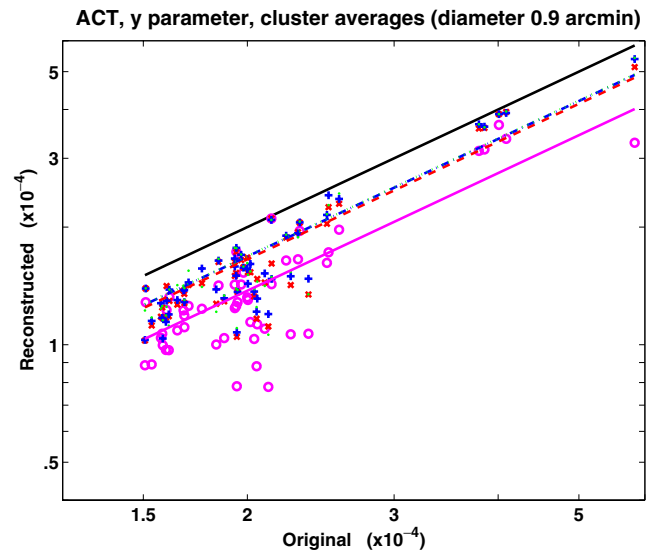


**Figure 7.** The input and output  $y$  parameters for bright clusters in the ACT experiment: top solid line, line of perfect reconstruction; circles, bottom solid line, Gaussian prior; plus symbols, dash-dotted line, profile prior; crosses, dashed line, profile d prior.



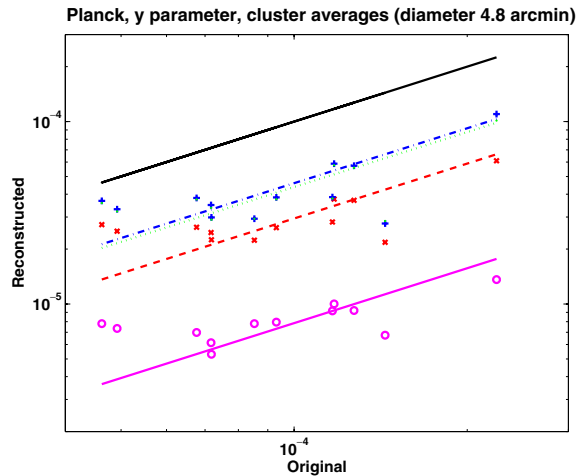


**Figure 8.** The input and output  $y$  parameters for bright clusters in the *Planck* experiment: top solid line, line of perfect reconstruction; circles, bottom solid line, Gaussian prior; plus symbols, dash-dotted line, profile prior; crosses, dashed line, profile d prior.

**Table 2.** The slope and the spread of the lines in Figs 7 and 8, obtained with different priors  $p_{\ln z}$ .

		Gaussian	Uniform	Profile	Profile d
Slope	ACT	0.69	0.84	0.84	0.83
	<i>Planck</i>	0.07	0.41	0.43	0.27
Spread	ACT	0.15	0.12	0.12	0.11
	<i>Planck</i>	0.35	0.27	0.27	0.31

The profile and uniform priors perform very similarly in reconstructing the cluster centres, so that we only quote the reconstruction parameters for the profile prior. It is comforting, however, that the details in the shape of the non-Gaussian profile play a minor role in the reconstruction performance.

### 4.3 Performances in the $y$ parameter reconstruction

We now come to the relevant question: which observable should be used in order to derive cosmological parameters? In particular, which should be the angle  $\theta_c$  over which the  $y$  parameter should be averaged? In general, we expect the answer to depend on the specific experiment in hand. In order to answer this question, we smoothed the input and reconstructed maps over several angles, and then we computed the slope of the reconstruction and the spread of the points around that slope.

Figs 9 and 10 show the slope and spread of the fitting as a function of the smearing angle for the ACT and *Planck* experiments, when the clusters in Figs 7 and 8 are considered.

As for the ACT case, we notice a big improvement when we reach the highest resolution of the instrument. At this  $\theta_c$ , the slope increases significantly (yielding almost perfect reconstruction, 0.8–0.9) and the spread is greatly reduced. Notice that for the ACT the method proposed here reduces the spread by about a factor of 2. The overall error in the reconstruction (10 per cent) should not present a major impediment in deriving cosmological parameters from this sample.

The beam size is also driving the spread associated with the slope, which drops dramatically for  $\theta_c \simeq 0.9$ . In order to better understand the role of the beam, we studied the idealistic case in which the

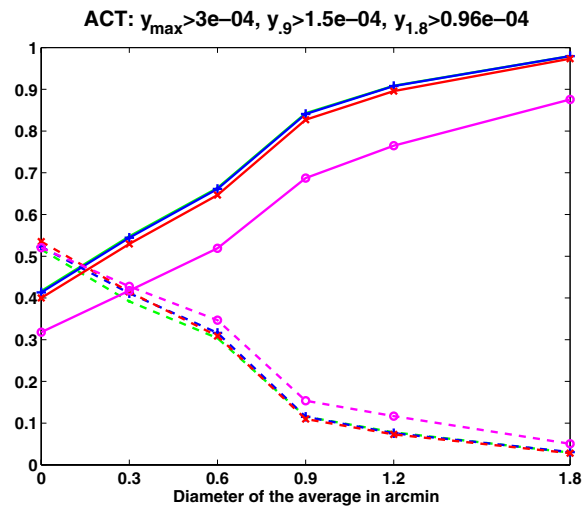


**Figure 9.** The slope (solid) and spread (dashed) of the fitting line for the input/output  $y$  parameter when averaged over different angles  $\theta_c$ . This plot is constructed using the 50 brightest clusters in 24  $(1.2\text{-deg})^2$  ACT maps.

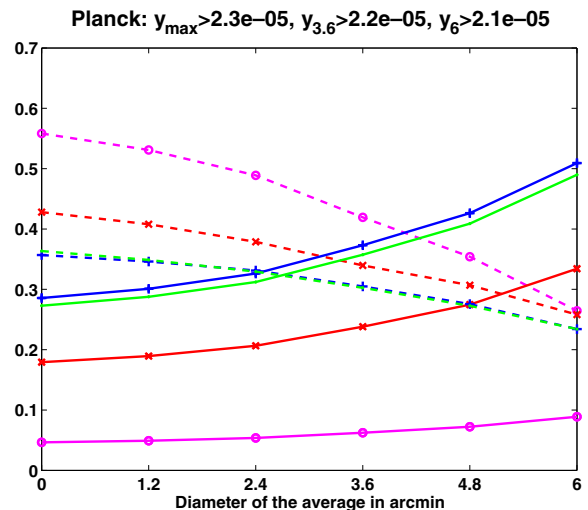


**Figure 10.** The slope (solid) and spread (dashed) of the fitting line for the input/output  $y$  parameter when averaged over different angles  $\theta_c$ . This plot is constructed using the 12 biggest clusters in  $(10\text{-deg})^2$  *Planck* maps.

beam is virtually zero (see Fig. 11). We find that in this limit, the Wiener filter reconstruction still shows a spread, while in our proposed model the spread is minimal. We conclude that should observational performances improve in the upcoming years, this method would become even more interesting.

Also in the case of *Planck* (Fig. 10), we see a significant improvement of this method on Wiener filtering in terms of the slope and the spread. However, the spread is still about 30 per cent, even for the most extended clusters considered here. Note also that these clusters were selected by being the biggest in the sample rather than the brightest, because some of the very compact bright clusters become completely confused with noise and are not reconstructed at all. This could be a potential problem when it comes to deriving the cosmological parameter from them. However, the real performances of the *Planck* instrument may be better than those used in this simulation. Moreover, the noise in the sky will not be uniformly distributed; in fact, some areas will be better sampled than others. We assessed

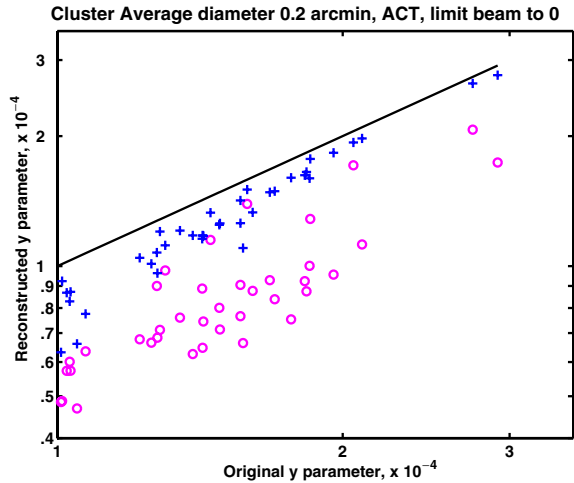


**Figure 11.** Reconstruction of the  $y$  parameter in the ACT experiment in the idealistic case where the beam is set to zero. The profile prior (plus symbols) significantly reduces the spread in the reconstructed  $y$  parameter with respect to the Gaussian prior (circle).

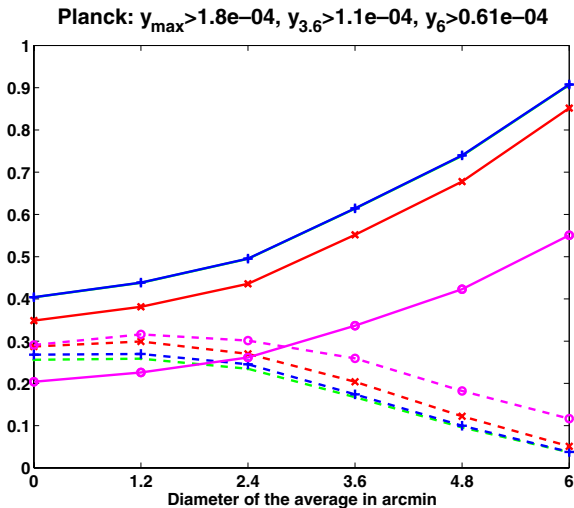


**Figure 12.** The slope (solid) and spread (dashed) of the fitting line for the input/output  $y$  parameter when averaged over different angles  $\theta$ . This plot is constructed using the 25 brightest clusters in the 10 *Planck* maps. In this case, the noise has been reduced by a factor of 7 in all frequency bands.

the relevance of the noise level by performing a similar analysis on the *Planck* maps with a reduced level of noise (about a factor of 7 lower). The results are displayed in Fig. 12 for the 25 brightest clusters in the *Planck* reconstructed maps. Here we appreciate that the noise is really the limiting factor for *Planck*; a significantly reduced noise would allow us to have almost perfect reconstruction of bright clusters with a spread reduced to 10 per cent. The critical issue now is how big will be the area of the sky where this performance will be achieved. Because the scanning strategy and the instrument performances are not settled yet, this is not a straightforward question to answer. It is clear, however, that the selection function for the *Planck* cluster catalogue will also depend on the reconstruction method and associated errors in different areas of the sky.

#### 4.4 Completeness and purity of the samples

Once a cluster map is reconstructed, it is sensible to ask whether the structures found really correspond to clusters in the input map or not. Furthermore, we would like to know if a given threshold in the reconstructed map can be associated with an input cluster intensity with high confidence. To this aim, we tried to assess the completeness and purity of our samples for given output intensities. In order to assess the purity/completeness in the ACT, we smoothed the maps to 0.9 arcmin and considered all local maxima in the reconstructed map which would have a cluster counterpart in the input one within a radius of 0.6 arcmin. We use the term ‘purity’ to indicate the fraction of the targeted clusters which do have a counterpart in the input map. We found that the purity is one for all relevant intensities, i.e. the reconstruction does not create clusters out of nothing, at least in the limit of the approximations applied here (i.e. no point sources). We then considered a given intensity in the input map, projected it into a reconstructed value using the slope calculated before and counted the fraction of objects that were effectively reconstructed above such threshold. We use the term ‘completeness’ to indicate the fraction of the initial clusters that make that threshold in the reconstructed map. The sample is complete for clusters with  $y$  parameter bigger than  $3 \times 10^{-4}$  (there are about 15 such clusters in a 100-deg<sup>2</sup> ACT survey). However, completeness drops to 50 per cent for  $y$  above  $1.5 \times 10^{-4}$  (about 150 such clusters in a 100-deg<sup>2</sup> ACT survey). This is because very compact clusters are anyway mapped into less intense objects; they would be accounted for if we considered the spread associated with the reconstruction.

As for *Planck*, we still have a very good purity level. However, the level of noise considered here prevents us from assessing completeness. The dimension of the cluster (rather than its intensity) seems to be the dominant factor in selecting the clusters that are reconstructed. This biases the reconstruction in favour of local clusters, rather than the most intense. Hopefully the real noise level will be better than that used here in most areas of the sky, so that a selection on the basis of brightness rather than size will be possible.

## 5 CONCLUSIONS

We have investigated the issue of SZ cluster reconstruction in future multifrequency CMB experiments. We have proposed a new method for component separation that is specifically tailored to reconstruct SZ galaxy clusters. Our approach takes into account that clusters produce a non-Gaussian, localized signal and they are non-spherical, sparse objects on the sky. The reconstruction is based in the wavelet domain, and therefore is local and takes into account covariances between different scales, positions and orientations. We have studied the performances of this estimator with different models of non-Gaussianity, some corresponding to that observed in SZ simulated maps and others that are common in image reconstruction literature. We show that this method outperforms previous techniques such as Wiener filtering in recovering the cluster central intensity, in terms of both average reconstruction and associated error. This result mainly depends on the better characterization of the bright pixel (corresponding to cluster centres) that we achieve with the non-Gaussian prior assumed. The success of this strategy depends on the combined effect of using a wavelet basis, a local reconstruction and an adequate non-Gaussian model for the signal.

We applied our method to two experiments, very different in nature: *Planck* and the ACT. In the case of the ACT, our method allows us to recover the 80–90 per cent of the central intensity of our 50 brightest reconstructed clusters with a reconstruction error of about 10 per cent (mainly caused by the beam size). The 100-deg<sup>2</sup>

ACT survey should contain about 150 such clusters, and the sub-sample with high completeness level should contain approximately 50 clusters. This is an adequate sample to constrain cosmology.

In the case of *Planck*, we were able to better reconstruct the most extended clusters, rather than the brightest. This method allows a reconstruction of 45 per cent of the cluster intensity, improving on standard Wiener filtering by about a factor of 5. The error associated with the reconstruction for the 12 targeted clusters is however still about 27 per cent. While this is an improvement on the Wiener filtering, it is somewhat unsatisfactory for deriving cosmology. Another limitation derives from the particular selection effect: most bright but compact clusters are not reconstructed at all. We point out that the major limitation for *Planck* is the noise level, and we show that a reduced noise level would allow almost perfect reconstruction with very little scatter for a sample of intensity-selected clusters. The area of the *Planck* sky where this will be possible depends upon the final scan strategy and instrument performance, which are not precisely defined yet. In general, we expect to have very different selection functions which will depend on sky positions; a detailed study like the present one will be necessary to infer actual performance.

These results may depend heavily on our neglect of point sources. It is important to point out however that the localized and non-Gaussian nature of the point source signal will almost certainly affect the standard Wiener filter techniques more adversely than the non-Gaussian estimator presented here. We will pursue this more in future research.

## ACKNOWLEDGMENTS

EP is a National Science Foundation (NSF) ADVANCE fellow (grant AST0340648), also supported by the National Aeronautics and Space Administration (NASA) grant NAG5-11489.

## REFERENCES

- Aghanim N., Kunz M., Castro P. G., Forni O., 2003, *A&A*, 406, 797  
 Battye R. A., Weller J., 2003, *Phys. Rev. D.*, 68, 083506  
 Bennett C. L. et al., 2003, *ApJS*, 148, 1

- Cayón L. et al., 2000, *MNRAS*, 315, 757  
 Cayón L., Sanz J. L., Martínez-González E., Banday A. J., Argüeso F., Gallegos J. E., Górski K. M., Hinshaw G., 2001, *MNRAS*, 326, 1243  
 Diego J. M., Vielva P., Martínez-González E., Silk J., Sanz J. L., 2002, *MNRAS*, 336, 1351  
 Diego J. M., Hansen S. H., Silk J., 2003, *MNRAS*, 338, 796  
 Herranz D., Sanz J. L., Hobson M. P., Barreiro R. B., Diego J. M., Martínez-González E., Lasenby A. N., 2002, *MNRAS*, 336, 1057  
 Hobson M. P., Jones A. W., Lasenby A. N., 1999, *MNRAS*, 309, 125  
 Hu W., 2003, *Phys. Rev. D.*, 67, 081304  
 Hufferberger K. M., Seljak U., 2004, *New Astron.*, submitted (astro-ph/0408066)  
 Levine E. S., Schulz A. E., White M., 2002, *ApJ*, 577, 569  
 Maisinger K., Hobson M. P., Lasenby A. N., 2004, *MNRAS*, 347, 339  
 Majumdar S., Mohr J. J., 2003, *ApJ*, 585, 603  
 Melin J.-B., Bartlett J. G., Delabrouille J., 2005, *A&A*, 429, 417  
 Pierpaoli E., Borgani S., Scott D., White M., 2003, *MNRAS*, 342, 163  
 Portilla J., Strela V., Wainwright M. S. E., 2003, *IEEE Trans. Image Proc.*, 12, 138  
 Romberg J., Wakin M., Choi H., Baraniuk R., 2003, in *SPIE Wavelets X, A Geometric Hidden Markov Tree Wavelet Model*. SPIE, San Diego  
 Spergel D. N. et al., 2003, *ApJS*, 148, 175  
 Starck J.-L., Aghanim N., Forni O., 2004, *A&A*, 416, 9  
 Stolyarov V., Hobson M. P., Ashdown M. A. J., Lasenby A. N., 2002, *ApJ*, 336, 97  
 Sunyaev R. A., Zel'dovich I. B., 1980, *ARA&A*, 18, 537  
 Tegmark M., Efstathiou G., 1996, *MNRAS*, 281, 1297  
 Tenorio L., Jaffe A. H., Hanany S., Lineweaver C. H., 1999, *MNRAS*, 310, 823  
 Vielva P., Martínez-González E., Cayón L., Diego J. M., Sanz J. L., Toffolatti L., 2001a, *MNRAS*, 326, 181  
 Vielva P., Barreiro R. B., Hobson M. P., Martínez-González E., Lasenby A. N., Sanz J. L., Toffolatti L., 2001b, *MNRAS*, 328, 1  
 Weller J., Battye R. A., 2003, *New Astron. Rev.*, 47, 775  
 White M., 2003, *ApJ*, 597, 650  
 White M., Majumdar S., 2004, *ApJ*, 602, 565  
 Zhang P., Pen U., Wang B., 2002, *ApJ*, 577, 555

This paper has been typeset from a  $\text{\TeX}/\text{\LaTeX}$  file prepared by the author.